Journal of
Materials Chemistry B

ROYAL SOCIETY OF CHEMISTRY

PAPER

View Article Online
View Journal | View Issue

Check for updates

Cite this: *J. Mater. Chem. B*, 2020, 8, 7453

Growth of large-scale MoS_2 nanosheets on double layered $ZnCo_2O_4$ for real-time *in situ* H_2S monitoring in live cells†

Veerappan Mani, *[ab] Shanthi Selvaraj,[cd] Nithiya Jeromiyas, [a] Sheng-Tung Huang,[a] Hiroya Ikeda,[d] Yasuhiro Hayakawa, [d] Suru Ponnusamy,[c] Chellamuthu Muthamizhchelvan*[c] and Khaled Nabil Salama *[b]

Received 5th May 2020,
Accepted 30th June 2020

DOI: 10.1039/d0tb01162b

rsc.li/materials-b

There is an urgent need to develop *in situ* sensors that monitor the continued release of H_2S from biological systems to understand H_2S-related pathology and pharmacology. For this purpose, we have developed a molybdenum disulfide supported double-layered zinc cobaltite modified carbon cloth electrode (MoS_2–$ZnCo_2O_4$–$ZnCo_2O_4$) based electrocatalytic sensor. The results of our study suggest that the MoS_2–$ZnCo_2O_4$–$ZnCo_2O_4$ electrode has excellent electrocatalytic ability to oxidize H_2S at physiological pH, in a minimized overpotential (+0.20 *vs.* Ag/AgCl) with an amplified current signal. MoS_2 grown on double-layered $ZnCo_2O_4$ showed relatively better surface properties and electrochemical properties than MoS_2 grown on single-layered $ZnCo_2O_4$. The sensor delivered excellent analytical parameters, such as low detection limit (5 nM), wide linear range (10 nM–1000 μM), appreciable stability (94.3%) and high selectivity (2.5-fold). The practicality of the method was tested in several major biological fluids. The electrode monitors the dynamics of bacterial H_2S in real-time for up to 5 h with good cell viability. Our research shows that MoS_2–$ZnCo_2O_4$–$ZnCo_2O_4$/carbon cloth is a robust and sensitive electrode to understand how bacteria seek to adjust their defense strategies under exogenously induced stress conditions.

1. Introduction

Most of the current sensors are normal sensors that can provide static information about a biological parameter at a certain time instant. However, many of the biological parameters are actually dynamic variables; their amount varies over time and depends on external stimuli. These biological variables require real-time sensors that can give continuous information at different times.[1–3] Hydrogen sulfide (H_2S) is one such dynamic parameter that plays significant roles in biological cells in regulating physiologically essential processes as a second chemical messenger.[4] H_2S is essential to modulate neurotransmission and relax muscles[5] and it exerts cardioprotective, anti-inflammatory, and anti-apoptotic effects on several organs including cardiovascular, central nervous system (CNS), and gastrointestinal systems.[6] The normal levels of endogenous H_2S productions are 10–100 μM and 50–160 μM in blood and CNS, respectively.[7] H_2S injections in controlled doses actually have potential therapeutic effects, so slow releasing H_2S drugs have the potential to treat certain cardiovascular, neurological, and carcinogenic diseases. However, abnormal H_2S levels are extremely detrimental and implicated in many diseases, such as Alzheimer's disease, chronic kidney disease, liver cirrhosis, and traumatic brain injury.[8,9] Serum H_2S level is a biomarker for cardiovascular diseases such as atherosclerosis, coronary heart disease, hypertension and chronic obstructive pulmonary disease.[10] Therefore, a sensitive real-time H_2S tracking tool is essential to continuously measure its release from biological media.[11] Electroanalytical methods can provide quantitative information about analytes in biochemical media with high spatial and temporal resolution for hours or even days, and are simple, cost-effective and derivatization-free.[12–14] Nevertheless, low sensitivity, selectivity, and inadequate reproducibility of the

---

[a] Institute of Biochemical and Biomedical Engineering, Department of Chemical Engineering and Biotechnology, National Taipei University of Technology, Taipei 106, Taiwan, Republic of China
[b] Sensors Lab, Advanced Membranes and Porous Materials Center, Computer, Electrical and Mathematical Science and Engineering Division, King Abdullah University of Science and Technology (KAUST), Saudi Arabia. E-mail: veerappan.mani@kaust.edu.sa, khaled.salama@kaust.edu.sa
[c] Centre for Nanoscience and Nanotechnology, Department of Physics and Nanotechnology, SRM Institute of Science and Technology, Tamil Nadu, India. E-mail: selvancm@gmail.com
[d] Research Institute of Electronics, Shizuoka University, 3-5-1 Johoku, Naka-ku, Hamamatsu, Japan

† Electronic supplementary information (ESI) available. See DOI: 10.1039/d0tb01162b

unmodified electrode resulting from poor surface properties of the bulk surface limit the full potential of electroanalytical methods.[15] The design and synthesis of advanced nanostructured materials is a facile method to tailor the surface properties of the electrodes.[16] Often, integrated hybrid electrode materials can meet the requirements of real-time *in situ* electrocatalytic sensors by combining the properties of all its components.[17,18]

Zinc cobaltite ($ZnCo_2O_4$), a mixed ternary metal oxide nanostructure, has attracted considerable interest in electrochemical applications due to its multiple redox reactions, expanded surface area, stability, and increased conductivity.[19,20] $ZnCo_2O_4$ has a similar cubic spinal crystal structure to Co_3O_4, and exhibits relatively better electrocatalytic activity, lower cost, and environmental benignity than Co_3O_4.[21] $ZnCo_2O_4$ can be prepared in different shapes such as, nanotubes,[22] microspheres,[23] nanoflowers,[24] and core–shell structures.[25] Besides, the hybridization of $ZnCo_2O_4$ with metal sulfides can produce efficient functional engineering materials with synergistic properties.[26,27] Although the applicability of such $ZnCo_2O_4$ materials has been demonstrated in energy devices, their use in biosensors is rarely explored.[28,29] On the other hand, electrode passivation is a major issue in fabricating reproducible H_2S sensors.[30] A surface preconditioning procedure is reported to eliminate the passivation issue by placing a layer of elemental sulfur on the electrode prior to measurement.[15] Here, we present an alternative approach based on the inherent property of molybdenum sulfide (MoS_2) material. We suggest that the presence of sulfur layers in MoS_2 sheets can help to overcome the sulfur deposition through repulsive interactions.[8] Unlike previous methods, this approach does not affect the conductivity of the working electrode. Moreover, MoS_2 nanosheets and its composites are critically acclaimed materials for electrocatalytic sensing applications.[31]

Here we report a synthesis flow for hierarchical MoS_2 decorated double-layered $ZnCo_2O_4$ nanostructures on top of a carbon cloth electrode for robust and sensitive H_2S detections. Carbon cloth is an inexpensive and flexible template with high mechanical strength. Its interconnected network assembly can provide rich active spots to grow nanomaterials.[32] As shown in Fig. 1, single-layered and double-layered $ZnCo_2O_4$ nanostructures were fabricated on a CC substrate. Then, a uniform layer of MoS_2 nanostructure was deposited to obtain MoS_2–$ZnCo_2O_4$/CC and MoS_2–$ZnCo_2O_4$–$ZnCo_2O_4$/CC electrodes. Our studies show that MoS_2–$ZnCo_2O_4$–$ZnCo_2O_4$/CC has relatively better surface properties and superior electrocatalytic ability compared to other electrodes. In addition, it displays several advantages over other materials, such as minimized overpotential, low detection limit, no pre-treatment, and functioning at physiological pH. MoS_2–$ZnCo_2O_4$–$ZnCo_2O_4$/CC can be used to establish a sensing platform for tracking H_2S release in *E. coli*. As the electrode is based on flexible carbon fabric, it can be a suitable candidate for wearable biosensing applications.[33]

2. Experimental

2.1. Materials and instrumentation

All the purchased chemicals were of analytical grade and used directly without any further purification. Zinc nitrate hexahydrate [$Zn(NO_3)_2 \cdot 6H_2O$], cobalt nitrate hexahydrate [$Co(NO_3)_2 \cdot 6H_2O$], urea [$CO(NH_2)_2$], ammonium fluoride [$(NH_4)F$], sodium molybdate [$Na_2MoO_4 \cdot 6H_2O$], and thiourea [CH_4N_2S] were purchased from Wako chemicals, Japan. Carbon cloth was provided by sainergy fuel cell India. The aqueous solution of H_2S was freshly prepared on the day of use by dissolving NaHS (purchased from Sigma) in deoxygenated PBS, sealing the container with a rubber septum, and purging the headspace with N_2. Instead of NaHS, the term H_2S has been used throughout the manuscript for clarity. A human blood sample was collected from a healthy human with consent. 0.1 M phosphate buffer saline (PBS), pH 7.4 was used as a supporting electrolyte. 0.1 M acetate buffer (with pH 4.4 & 5.4), 0.1 M phosphate buffer (with pH 6.4), 0.1 M PBS (with pH 7.4), and 0.1 M Tris-buffer saline (with pH 8.4 & 9.4) were used for a pH optimization test. All studies were performed three times and the average of three readings was used to plot the data.

The electrochemical experiments were performed with a CHI 612D electrochemical workstation (CH Instruments, Inc., U.S.A). FE-SEM characterization were performed using a JSM-7001F instrument. X-ray diffraction (XRD) studies were performed using an RINT-2200 diffractometer, Rigaku, Japan, CuKα radiation, λ = 1.54178 Å. Raman spectra were acquired using NRS-7100 with a laser excitation wavelength of 532 nm (spot size 1 μm). An EIM6ex Zahner (Kronach, Germany) was used for electrochemical impedance spectroscopy (EIS) studies. EIS parameters are, bias potential = 0 V, amplitude = 5 mV, and frequency = 100 mHz to 100 kHz. X-ray photoelectron spectra

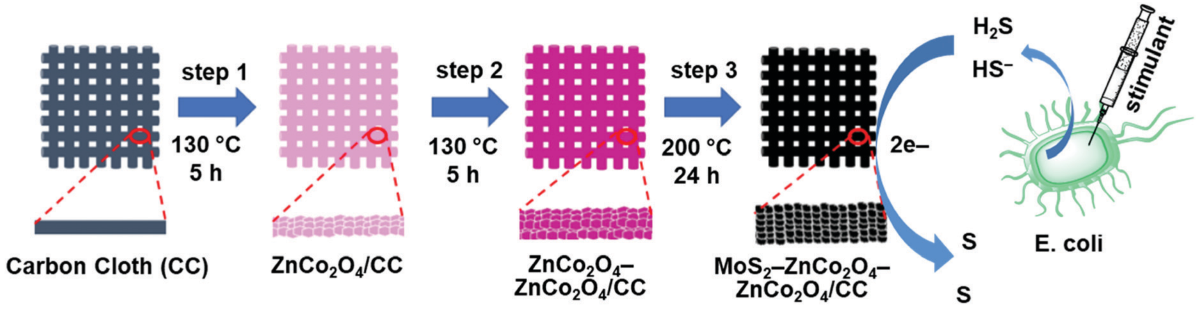

Fig. 1 Schematic illustration of the fabrication process: step 1: hydrothermal growth of single layered $ZnCo_2O_4$ on CC, step 2: hydrothermal growth of double layered $ZnCo_2O_4$ on CC, step 3: hydrothermal growth of MoS_2 on double layered $ZnCo_2O_4$/CC.

(XPS) were obtained by using a Shimadzu ESCA 3100. The counting of bacterial cells was performed using a spectrophotometer fitted with a xenon lamp and 1.0 cm quartz cells.

2.2. Fabrication of single layered $ZnCo_2O_4$ nanosheets on carbon cloth – step 1

Carbon cloth (CC: 2 cm × 2 cm) was pre-cleaned with 3 M HCl solution for about 10 min to remove exterior filth and cleaned with DI water & ethanol for about thrice the time. In the fabrication process, 3 mM $Zn(NO_3)_2{\cdot}6H_2O$, 6 mM $Co(NO_3)_2{\cdot}6H_2O$, 10 mM NH_4F and 15 mM $Co(NH_2)_2$ were liquified in 80 mL DI water and stirred for about 30 min to attain the homogeneous mixture solution. The prepared homogeneous mixture solution was moved to a Teflon-lined stainless steel autoclave with the pre-cleaned CC substrate and sustained at 130 °C for 5 h. After cooling down to room temperature, the fabricated $ZnCo_2O_4$/CC was washed with DI water and ethanol and dried at 90 °C overnight. After the drying process, the electrode was subjected to a calcination process at 200 °C for 5 h under atmospheric conditions.

2.3. Fabrication of double layered $ZnCo_2O_4$ nanosheets on carbon cloth – step 2

In the fabrication process, 3 mM $Zn(NO_3)_2{\cdot}6H_2O$, 6 mM $Co(NO_3)_2{\cdot}6H_2O$, 10 mM NH_4F and 15 mM $Co(NH_2)_2$ were liquified in 80 mL DI water and stirred for about 30 min to attain the homogeneous mixture solution. The prepared homogeneous solution was transferred to a Teflon lined stainless steel autoclave with the $ZnCo_2O_4$/CC and maintained at 130 °C for 5 h. After cooling down to room temperature, the fabricated $ZnCo_2O_4$–$ZnCo_2O_4$/CC was prudently washed with DI water & ethanol several times and dried at 90 °C overnight. After drying, the electrode was subjected to calcination at 200 °C for 5 h.

2.4. Fabrication of MoS_2 nanosheets–$ZnCo_2O_4$–$ZnCo_2O_4$ on carbon cloth – step 3

In the fabrication process, 2 mM $Na_2MoO_4{\cdot}6H_2O$ and 13 mM CH_4N_2S were liquefied in 80 mL DI water and stirred for about 30 min to attain a homogeneous mixture. The mixture was transferred to a Teflon-lined stainless steel autoclave with fabricated electrode material $ZnCo_2O_4$–$ZnCo_2O_4$/CC and sustained at 200 °C for about 24 h. After cooling down to room temperature, the fabricated MoS_2–$ZnCo_2O_4$–$ZnCo_2O_4$/CC was washed with water and ethanol several times and dried at 90 °C overnight. After the drying process, the fabricated electrode materials were subjected to calcination at 200 °C for 5 h to yield MoS_2–$ZnCo_2O_4$–$ZnCo_2O_4$/CC. In parallel, MoS_2 was also deposited on a single-layered $ZnCo_2O_4$ to prepare MoS_2–$ZnCo_2O_4$/CC.

Finally, a thin layer of polymerized *o*-phenylenediamine (POPD) was deposited on the MoS_2–$ZnCo_2O_4$–$ZnCo_2O_4$/CC through voltammetric deposition. This coating is useful to enable anti-fouling properties against biological species and to provide H_2S permselective properties to the electrode.[15] To perform this step, the electrode (MoS_2–$ZnCo_2O_4$–$ZnCo_2O_4$/CC or MoS_2–$ZnCo_2O_4$/CC) was transferred into an electrochemical cell containing 10 mM *o*-phenylenediamine suspended in PBS (pH 7.4) and 2 cycles of cyclic voltammograms were ramped at 0.025 V s^{-1} scan rate between 0 V and 1.0 V. The POPD coated electrode was carefully washed with water and dried under ambient conditions before being used for sensing study.

2.5. Bacteria cell culture

E. coli strain MG1655 was grown on a Lysogeny broth (LB) agar plate. The growth period was overnight and the temperature was maintained at 37 °C. A single colony of the as-grown *E. coli* was inoculated in 20 mL of LB medium and the incubation was maintained overnight at 37 °C. Constant shaking was applied for both the incubation processes. The cell counts were estimated by spectrophotometer analysis (optical density, OD_{600} = 0.65 at 37 °C). The bacterial solution was diluted with fresh LB medium with a ratio of 1 : 9. The bacterial count was calculated to be 2.5×10^9 cells per mL *via* cytometry.

2.6. Electrochemical experiments in *E. coli*

2.5×10^9 cells per mL of *E. coli* in a 20 mL LB medium (pH 7.4) was transferred to a typical electrochemical cell. Three electrodes were immersed in the cell: MoS_2–$ZnCo_2O_4$–$ZnCo_2O_4$/CC was the working electrode, Ag/AgCl was the reference electrode and Pt was the counter electrode. The chronoamperometric experiments were conducted at a constant potential of +0.20 V for 100 s. The steady-state currents were used to make calibration plots.

3. Results and discussions

The schematic representation for the fabrication process of hierarchical nanoarchitectures of MoS_2–$ZnCo_2O_4$–$ZnCo_2O_4$ on flexible carbon cloth is illustrated in Fig. 1. The mechanism of nucleation and the subsequent growth process of the $ZnCo_2O_4$ nanosheets are represented below. Initially, the $Zn_xCo_{2x}(OH)_{6x}$ precursor nanoparticles were produced by the hydrolysis of urea ($Co(NH_2)_2$), during the hydrothermal process of dissociation of Zn^{2+} and Co^{2+} ions with OH^- ions. The formed $Zn_xCo_{2x}(OH)_{6x}$ precursor nanoparticles may stick to the flexible CC substrate and be loaded upon one another. Then, the formed $Zn_xCo_{2x}(OH)_{6x}$ precursor nanoparticles grew into thin layered nanosheets, which is driven by the minimization of the surface energy. The $Zn_xCo_{2x}(OH)_{6x}$ precursor nanoparticles can be easily transformed to $ZnCo_2O_4$ through the subsequent annealing process. The as-deposited thin single and double layered $ZnCo_2O_4$ nanosheets were used as a template, by providing plentiful active nucleation spots for successive progress of MoS_2.

By the ensuing hydrothermal process with MoS_2 precursor solution from $Na_2MoO_4{\cdot}6H_2O$ and CH_4N_2S, MoS_2 nanocrystals were initially formed on the surface of thin single and double layered $ZnCo_2O_4$ nanosheets. Later, these MoS_2 nanocrystals further grew into interconnected MoS_2 nanosheets, resulting in the formation of nanoarchitectures on a flexible CC substrate. The possible mechanism for the formation of MoS_2–$ZnCo_2O_4$–$ZnCo_2O_4$/CC is shown in the following equations:[34]

The formation of $ZnCo_2O_4$ is represented as:

$$Co(NH_2)_2 + H_2O \rightarrow C_3H_6N_6 + 6NH_3 + 3CO_2 \tag{1}$$

$$NH_3 + NH_4F + H_2O \rightarrow 2NH^{4+} + OH^- + F^- \tag{2}$$

$$xZn^{2+} + 2xCo^{2+} + 6xOH^- \rightarrow Zn_xCo_{2x}(OH)_{6x} \tag{3}$$

$$Zn_xCo_{2x}(OH)_{6x} + 0.5xO_2 \rightarrow xZnCo_2O_4 + 3xH_2O \tag{4}$$

The formation of MoS_2 is represented as:

$$SC(NH_2)_2 + 2H_2O \rightarrow CO_2 + 2NH_3 + H_2S \tag{5}$$

$$H_2S \rightarrow 2H^+ + S^{2-} \tag{6}$$

$$4MoO_4{}^{2-} + 9S^{2-} + 24H^+ \rightarrow 4MoS_2 + 12H_2O + SO_4{}^{2-} \tag{7}$$

3.1. Improved surface properties of MoS_2–$ZnCo_2O_4$–$ZnCo_2O_4$/CC over MoS_2–$ZnCo_2O_4$/CC

Fig. 2A and B display the FE-SEM image of single-layered $ZnCo_2O_4$ nanosheets on carbon cloth, which clearly shows that the entire CC is fully covered with uniform and aligned thin $ZnCo_2O_4$ nanosheets. Fig. 2C and D show the FE-SEM image of $ZnCo_2O_4$–$ZnCo_2O_4$ hierarchical nanosheets. The aligned double-layered $ZnCo_2O_4$ nanosheets are much denser, uniform and homogeneous than the aligned single-layered $ZnCo_2O_4$ nanosheets. In addition, the surface of the double-layered $ZnCo_2O_4$ nanosheets is rougher than the single-layered $ZnCo_2O_4$ nanosheets. The inner layer of $ZnCo_2O_4$ and outer layer $ZnCo_2O_4$ are expected to have different dimensions and aspect ratios, because of the utilization of different substrates as templates; *i.e.*, CC and $ZnCo_2O_4$/CC, during the step-1 and step-2 hydrothermal approaches. No $ZnCo_2O_4$ was crammed in the inter-space region of the nanostructure-interconnected assembly, signifying that outer $ZnCo_2O_4$ layer was fully-fledged on the exterior of the innermost $ZnCo_2O_4$ thin nanosheets.

Fig. 2E and F show the FE-SEM images of MoS_2-single layered $ZnCo_2O_4$ nanosheets attained through the step-3 hydrothermal approach, with the aligned thin single layered nanosheets like $ZnCo_2O_4$/CC as the substrate. Fig. 2G and H display the typical FE-SEM image of MoS_2–$ZnCo_2O_4$–$ZnCo_2O_4$ nanoarchitectures accomplished through the step-3 hydrothermal approach, with the aligned thin double-layered $ZnCo_2O_4$–$ZnCo_2O_4$/CC as the substrate. Large scale interconnected MoS_2 nanosheets grew uniformly and densely on both the single layered and double layered $ZnCo_2O_4$ nanosheets on a CC substrate. With the help of $ZnCo_2O_4$ nanosheets, the interconnected MoS_2 can assemble on both sides of the $ZnCo_2O_4$ sheets in hierarchical porous overlays. Such hybrid nanosystems can efficiently facilitate charge transport at the interface.

3.2. Crystal structure, elemental analysis, and binding studies

Fig. 3A displays the XRD patterns of $ZnCo_2O_4$/CC, $ZnCo_2O_4$–$ZnCo_2O_4$/CC, MoS_2–$ZnCo_2O_4$/CC and MoS_2–$ZnCo_2O_4$–$ZnCo_2O_4$/CC. From the XRD peak patterns of $ZnCo_2O_4$/CC and $ZnCo_2O_4$–$ZnCo_2O_4$/CC, the diffraction crystal planes (311), (400), (220), (222), (422), and (440) could be indexed to a cubic crystal spinel structure of $ZnCo_2O_4$ (JCPDS No. 23-1390).[35] From the XRD peak patterns of MoS_2–$ZnCo_2O_4$/CC and MoS_2–$ZnCo_2O_4$–$ZnCo_2O_4$/CC, the diffraction crystal planes (002), (004) and (100) could be indexed to MoS_2 nanostructures (JCPDS No. 37-1492). No other peaks indexed to impurities are detected from the XRD curves, indicating the formation of an electrode with high crystallization and purity.

Fig. 3B displays the Raman spectra of $ZnCo_2O_4$/CC, $ZnCo_2O_4$–$ZnCo_2O_4$/CC, MoS_2–$ZnCo_2O_4$/CC and MoS_2–$ZnCo_2O_4$–$ZnCo_2O_4$/CC. Four peaks at 195, 474, 510 and 679 cm^{-1} were observed in the Raman spectra of $ZnCo_2O_4$/CC and $ZnCo_2O_4$–$ZnCo_2O_4$/CC, assigned to the characteristic modes of $ZnCo_2O_4$ nanostructures with the vibrational modes of F_{2g}, E_g, F_{2g} and A_{1g}, respectively.[26] An additional two peaks are observed for the Raman spectra of MoS_2–$ZnCo_2O_4$/CC and MoS_2–$ZnCo_2O_4$–$ZnCo_2O_4$/CC at 382.4 and 407.6 cm^{-1}, which are recognized as the E^1_{2g} and A_{1g} vibration modes of MoS_2, respectively.[36]

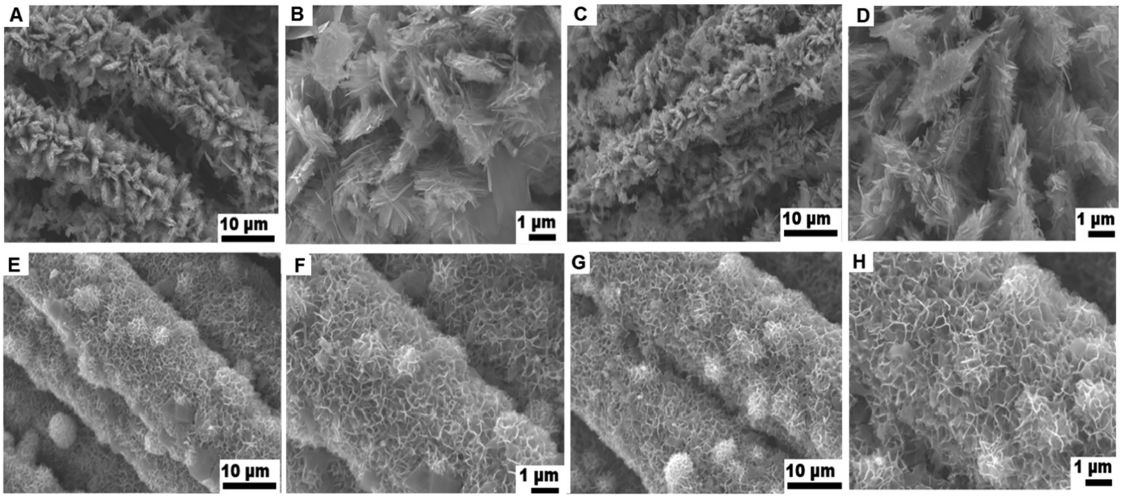

Fig. 2 FE-SEM images of single-layered $ZnCo_2O_4$/CC (A and B), double-layered $ZnCo_2O_4$–$ZnCo_2O_4$/CC (C and D), MoS_2–$ZnCo_2O_4$/CC (E and F) and MoS_2–$ZnCo_2O_4$–$ZnCo_2O_4$/CC (G and H).

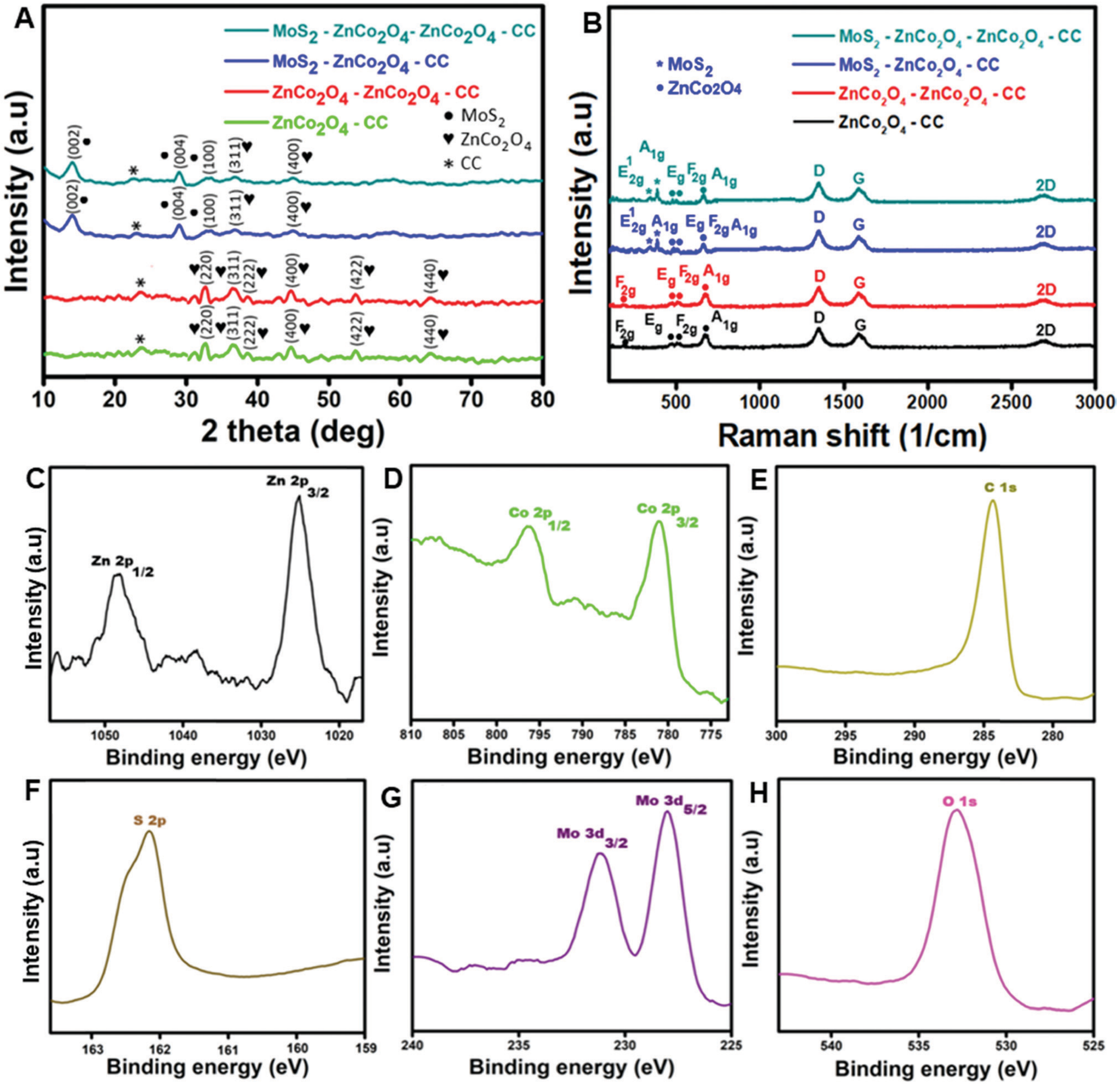

Fig. 3 (A) XRD curves of $ZnCo_2O_4$/CC, $ZnCo_2O_4$–$ZnCo_2O_4$/CC, MoS_2–$ZnCo_2O_4$/CC and MoS_2–$ZnCo_2O_4$–$ZnCo_2O_4$/CC. (B) Raman spectra of $ZnCo_2O_4$/CC, $ZnCo_2O_4$–$ZnCo_2O_4$/CC, MoS_2–$ZnCo_2O_4$/CC and MoS_2–$ZnCo_2O_4$–$ZnCo_2O_4$/CC. XPS analysis of the MoS_2–$ZnCo_2O_4$–$ZnCo_2O_4$/CC electrode: (C) Zn 2p, (D) Co 2p, (E) C 1s, (F) S 2p, (G) Mo 3d, and (H) O 1s.

Fig. 3C–H depict the XPS analysis of the MoS_2–$ZnCo_2O_4$–$ZnCo_2O_4$/CC electrode material. From Fig. 3C, the electronic configuration of Zn 2p identified at 1025.3 (Zn $2p_{3/2}$) and 1048.3 (Zn $2p_{1/2}$) eV, with an energy level difference of about 23.0 eV substantiated the presence of Zn ions with 2+ oxidation states.[37] From Fig. 3D, the electronic configuration of Co 2p acknowledged at 781 and 797 eV is assigned to Co $2p_{3/2}$ and Co $2p_{1/2}$, respectively. From Fig. 3E, the standard carbon peak achieved at 284.7 eV can be allocated to C 1s spectra. From Fig. 3F, a strong peak appeared at 162.2 eV assigned to S 2p spectra. From Fig. 3G, the peaks attained at 33 and 229 eV, are assigned to Mo 3d3/2 and Mo 3d5/2.[38] From Fig. 3H, a strong peak obtained at 532 eV is allocated to O 1s spectra.

3.3. Voltammetric behavior of the electrodes

Fig. 4A and B display the CV curves of $ZnCo_2O_4$–CC and $ZnCo_2O_4$–$ZnCo_2O_4$/CC, at an applied potential window between −0.25 V and +0.25 V with varying scan rates from 5 to 100 mV s^{-1}. 0.1 M KOH was used as a supporting electrolyte. All the CV curves displayed a pseudocapacitive nature and the redox peaks are mostly generated owing to the faradaic electrochemical reactions that are related to the representation as M-O/M-O-OH, where M is denoted as Zn^{2+} and Co^{2+}, which are associated with the OH^- anions.[39] The eqn (8)–(10) express the possible redox reactions that occur during the electrochemical process at the outer surface of MoS_2–$ZnCo_2O_4$–$ZnCo_2O_4$/CC.

$$ZnCo_2O_4 + H_2O + e^- \leftrightarrow 2CoOOH + Zn(OH)^- \quad (8)$$

$$CoOOH + OH^- \leftrightarrow CoO_2 + H_2O + e^- \quad (9)$$

$$ZnOH + OH^- \leftrightarrow Zn(OH)_2 + e^- \quad (10)$$

The CV area for the double-layered $ZnCo_2O_4$ electrode was much larger than that of the single-layered $ZnCo_2O_4$, revealing that the double-layered $ZnCo_2O_4$/CC hierarchical electrode has higher electrochemical activity than the single layered $ZnCo_2O_4$/CC (Fig. 4C).[40] A thin outer layer of porous $ZnCo_2O_4$ with enormous surface area favors fine ion diffusion at the electrolyte/electrode interface, which can provide more electrochemical active surface area for electrochemical reactions. Because of the rational design of double-layered $ZnCo_2O_4$/CC, it could achieve the greatest use of each layer of active material. Besides, the CV areas for the fabricated electrode materials are entirely different, because of the polarization effect, which is thoroughly linked to the structural morphology of the electrode materials.[41] Additionally, the resulting synergy effect of the double layered $ZnCo_2O_4$/CC hierarchical electrode affords an efficient pathway for ion and electron transport, during the electrochemical analysis.

Fig. 4D and E display the CV curves of MoS_2–$ZnCo_2O_4$/CC and MoS_2–$ZnCo_2O_4$–$ZnCo_2O_4$/CC with varying scan rate measurement values from 5 to 100 mV s^{-1}. 0.1 M KOH was used as a supporting electrolyte. CV curves display quasi-rectangular shapes, demonstrating the presence of dual electrochemical behavior of both electrochemical double layer capacitance and the pseudocapacitive nature of the fabricated electrode materials. No redox peaks were observed in the CV curves obtained with a KOH electrolyte, because of the development of a double layer at the interface of the electrode and electrolyte. Additionally, the CV area for electrode MoS_2–$ZnCo_2O_4$–$ZnCo_2O_4$/CC was much larger than that of the MoS_2–$ZnCo_2O_4$/CC, revealing that the double layered $ZnCo_2O_4$/CC has higher electrochemical activity than the single-layered $ZnCo_2O_4$/CC, as expressed in Fig. 4F. During the electrochemical process, the K^+ ions may diffuse into the surface of a MoS_2 layer as represented in eqn (11),

$$(MoS_2)\ surface + K^+ + e^- \leftrightarrow (MoS_2 + K^+)\ surface + e^- \quad (11)$$

Moreover, a CV rectangular curve with slight variation in the fabricated hybrid electrodes, MoS_2–$ZnCo_2O_4$/CC and MoS_2–$ZnCo_2O_4$–$ZnCo_2O_4$/CC for all scan rate measurements is primarily owing to reversible redox reactions of Mo^{3+}/Mo^{2+} linked with the OH^- ions. Eqn (12) and (13) show the possible redox reactions of MoS_2–$ZnCo_2O_4$/CC and MoS_2–$ZnCo_2O_4$–$ZnCo_2O_4$/CC,

$$MoS_2 + OH^- \leftrightarrow MoSOH + e^- \quad (12)$$

$$MoSOH + OH^- \leftrightarrow MoSO + H_2O + e^- \quad (13)$$

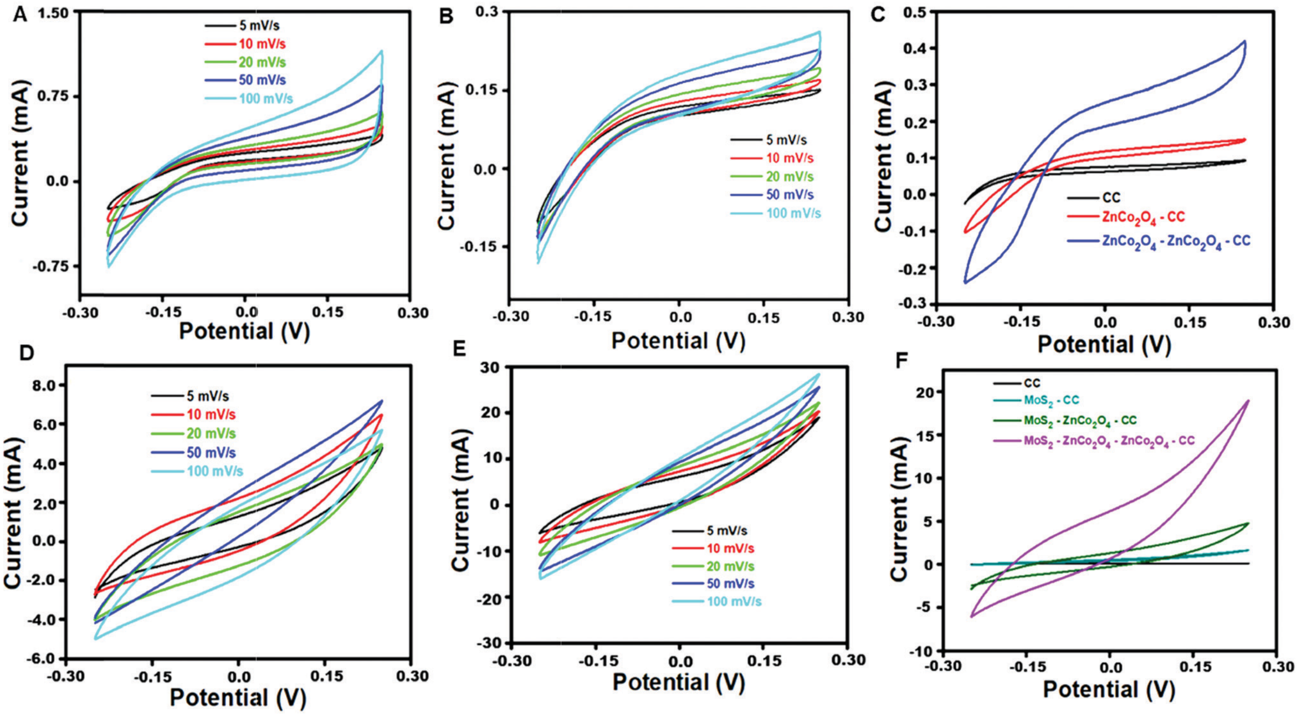

Fig. 4 CV curves of (A) $ZnCo_2O_4$/CC and (B) $ZnCo_2O_4$–$ZnCo_2O_4$/CC at different scan rates (5 to 100 mV s^{-1}). (C) Comparison of CV curves of CC, $ZnCo_2O_4$/CC, and $ZnCo_2O_4$–$ZnCo_2O_4$/CC at a scan rate of 5 mV s^{-1}. (D) CV plots of MoS_2–$ZnCo_2O_4$/CC and (E) MoS_2–$ZnCo_2O_4$–$ZnCo_2O_4$/CC at different scan rates (5 to 100 mV s^{-1}). (F) Comparison of CV curves of MoS_2/CC, MoS_2–$ZnCo_2O_4$/CC, and MoS_2–$ZnCo_2O_4$–$ZnCo_2O_4$/CC at a scan rate of 5 mV s^{-1}.

The electrochemically effective surface areas of $ZnCo_2O_4$/CC, $ZnCo_2O_4$–$ZnCo_2O_4$/CC, MoS_2–$ZnCo_2O_4$/CC and MoS_2–$ZnCo_2O_4$–$ZnCo_2O_4$/CC have been calculated by studying their electrochemical properties in the presence of $K_3[Fe(CN)_6]$ redox mediator. The Randles–Sevcik equation was used to calculate the active surface areas.[42,43] The active surface areas of $ZnCo_2O_4$/CC, $ZnCo_2O_4$–$ZnCo_2O_4$/CC, MoS_2–$ZnCo_2O_4$/CC and MoS_2–$ZnCo_2O_4$–$ZnCo_2O_4$/CC were found to be 0.672 cm^2, 0.750 cm^2, 0.842 cm^2, and 0.984 cm^2 respectively. MoS_2–$ZnCo_2O_4$–$ZnCo_2O_4$/CC has the largest active surface in comparison with other electrodes, which is in line with CV and EIS results.

3.4. MoS_2–$ZnCo_2O_4$–$ZnCo_2O_4$/CC has excellent interfacial electron transfer properties

Fig. 5 displays the EIS-Bode plot analysis of $ZnCo_2O_4$/CC (A), $ZnCo_2O_4$–$ZnCo_2O_4$/CC (B), MoS_2–$ZnCo_2O_4$/CC (C) and MoS_2–$ZnCo_2O_4$–$ZnCo_2O_4$/CC (D). From Fig. 5A–D, at 1 Hz frequency, the attained phase angles of $ZnCo_2O_4$/CC, $ZnCo_2O_4$–$ZnCo_2O_4$/CC, MoS_2–$ZnCo_2O_4$/CC and MoS_2–$ZnCo_2O_4$–$ZnCo_2O_4$/CC are represented as 60.9°, 58.5°, 19.68° and 15.6°, respectively. During the electrochemical process, larger phase shift values are observed for the electrodes, which is due to the charge transfer mechanism of different kinds of active materials.[44] The MoS_2–$ZnCo_2O_4$–$ZnCo_2O_4$/CC electrode showed better phase angle compared to other electrodes, suggesting superior electron transfer at this interface. Fig. 5E and F compare the Nyquist plots of $ZnCo_2O_4$/CC, $ZnCo_2O_4$–$ZnCo_2O_4$/CC, MoS_2–$ZnCo_2O_4$/CC and MoS_2–$ZnCo_2O_4$–$ZnCo_2O_4$/CC. The attained equivalent series resistance (ESR) values for the electrode materials $ZnCo_2O_4$/CC, $ZnCo_2O_4$–$ZnCo_2O_4$/CC, MoS_2–$ZnCo_2O_4$/CC and MoS_2–$ZnCo_2O_4$–$ZnCo_2O_4$/CC are, 2.9 Ω, 2.4 Ω, 1.3 Ω and 0.24 Ω, respectively. These electrodes have excellent electronic conductivity, as the $ZnCo_2O_4$ and MoS_2 arrays tightly attached to the carbon cloth to form very good adhesion and electrical contact, creating a smoother pathway for interface electron transfer. While comparing the ESR values of the above fabricated electrode materials, the MoS_2–$ZnCo_2O_4$–$ZnCo_2O_4$ has exhibited lower resistance values than other electrode materials, revealing the fast electron transfer at this interface. Thus, the double-layered $ZnCo_2O_4$ facilitates better electrochemical properties for the electrode compared to single layered $ZnCo_2O_4$, which is also in agreement with surface morphology results.

3.5. MoS_2–$ZnCo_2O_4$–$ZnCo_2O_4$/CC: an excellent electrocatalyst for H_2S oxidation

Next, the H_2S sensing aptitudes of the electrodes were tested by cyclic voltammetry. The potential was cycled between −0.50 V and + 0.50 V with a scan rate of 50 mV s^{-1}. Fig. 6A shows the CVs of MoS_2–$ZnCo_2O_4$–$ZnCo_2O_4$/CC in the absence (curve a′) and presence (curve b′) of 1 mM H_2S. In the absence of H_2S, the CV of MoS_2–$ZnCo_2O_4$–$ZnCo_2O_4$/CC displayed peaks corresponding to characteristic redox reactions of the nanomaterial, as explained in eqn (8)–(10). However, a large increase in peak current at +0.30 V with an onset potential of + 0.20 V was observed in the presence of H_2S. The dissolved H_2S and HS^- are the major forms of H_2S at pH 7.4 and fortunately both of them are electrochemically active.[15] They can undergo a two-electron oxidation process as given in eqn (14) and (15).

$$H_2S \rightarrow S^0 + 2e^- + 2H^+ \tag{14}$$

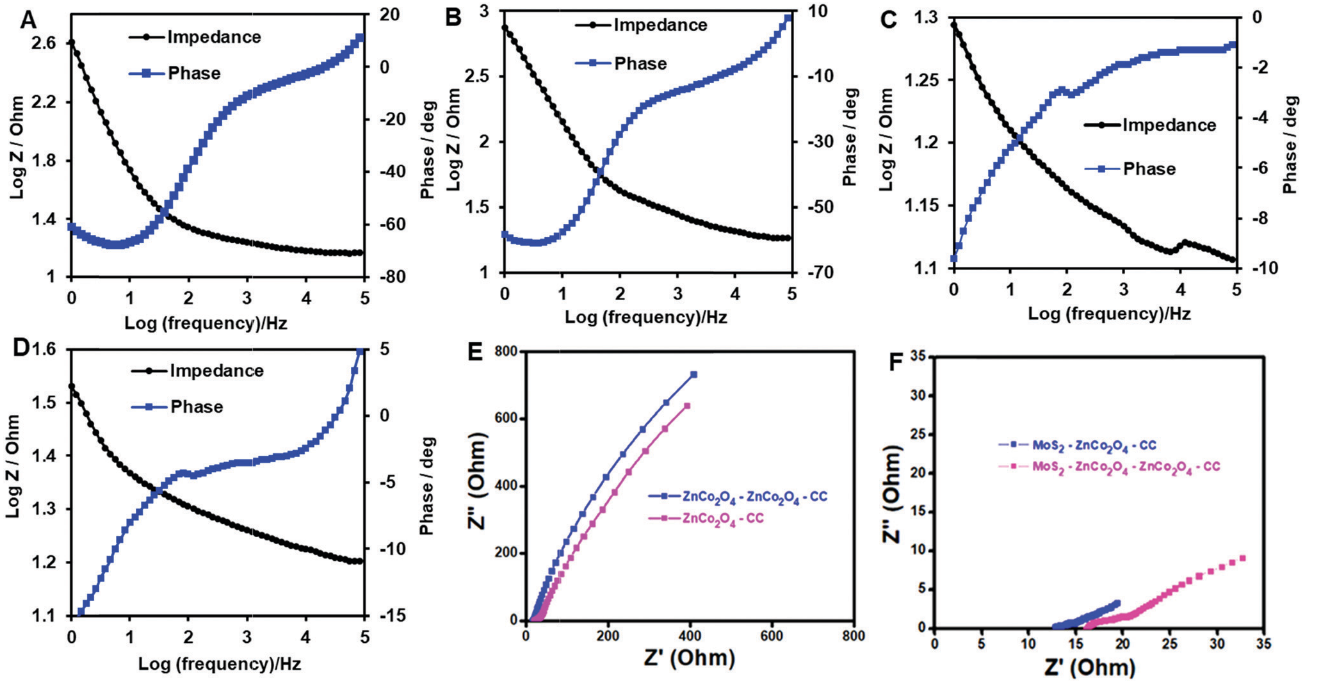

Fig. 5 EIS – Bode plot of $ZnCo_2O_4$/CC (A), $ZnCo_2O_4$–$ZnCo_2O_4$/CC (B), MoS_2–$ZnCo_2O_4$/CC (C), and MoS_2–$ZnCo_2O_4$–$ZnCo_2O_4$/CC (D). (E) EIS – Nyquist plot comparison of $ZnCo_2O_4$/CC and $ZnCo_2$O4–$ZnCo_2O_4$/CC. (F) EIS – Nyquist plot comparison of MoS_2–$ZnCo_2O_4$/CC and MoS_2–$ZnCo_2O_4$–$ZnCo_2O_4$/CC.

$$HS^- \rightarrow S^0 + 2e^- + H^+ \quad (15)$$

Fig. 6B compares the electrocatalytic responses of MoS_2–$ZnCo_2O_4$–$ZnCo_2O_4$/CC with unmodified CC, $ZnCo_2O_4$–$ZnCo_2O_4$/CC, and MoS_2–$ZnCo_2O_4$/CC. The bar diagram presented as an inset to Fig. 6B compares the response currents of the electrodes. The H_2S oxidation peak current at MoS_2–$ZnCo_2O_4$–$ZnCo_2O_4$/CC was 0.5, 1.4, and 2.2 folds higher than the MoS_2–$ZnCo_2O_4$/CC, $ZnCo_2O_4$–$ZnCo_2O_4$/CC and unmodified CC, respectively. The oxidation potential at MoS_2–$ZnCo_2O_4$–$ZnCo_2O_4$/CC was 0.33 V, 0.35 V, and 0.37 V lower than that at MoS_2–$ZnCo_2O_4$/CC, $ZnCo_2O_4$–$ZnCo_2O_4$/CC and unmodified CC, respectively. The minimized overpotential is highly useful in constructing a sensor without interference from common biological species. Notably, MoS_2–$ZnCo_2O_4$–$ZnCo_2O_4$/CC showed relatively better performance than the MoS_2–$ZnCo_2O_4$/CC, which indicates the significant role of double-layered $ZnCo_2O_4$. In accordance with the SEM and voltammetric results, we infer that the improved surface properties, such as surface area, roughness and porosity are the major reasons for the improved electrochemical properties. A typical electrochemical-coupled chemical (EC) reaction mechanism is proposed in the literature for H_2S oxidation at chemically modified electrodes such as MoS_2–$ZnCo_2O_4$–$ZnCo_2O_4$/CC.[45] The possible electrocatalytic mechanism involving the active nanomaterials can be given as eqn (16)–(19),

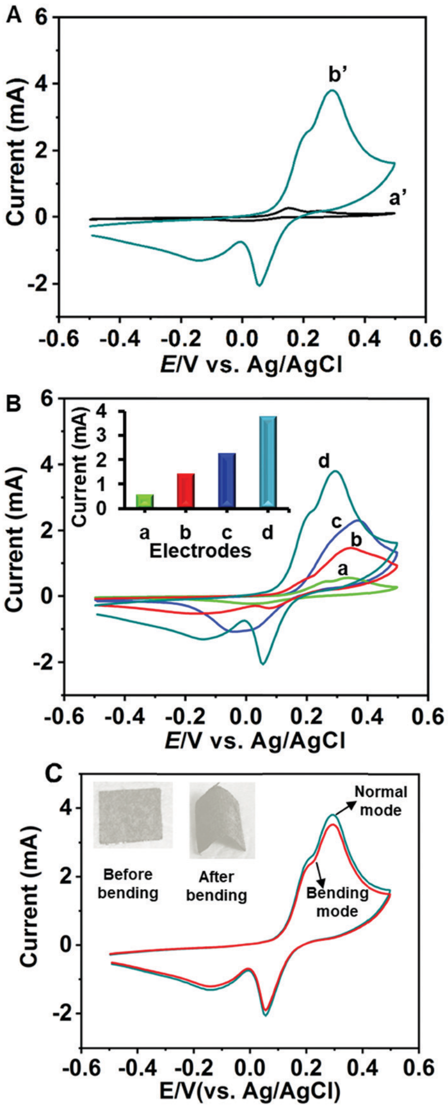

Fig. 6 (A) CV response of MoS_2–$ZnCo_2O_4$–$ZnCo_2O_4$/CC in the absence (a′) and presence (b′) of 1 mM H_2S suspended in 0.1 M PBS (pH 7.4). Scan rate = 50 mV s^{-1}. (B) CV responses of unmodified CC (a), $ZnCo_2O_4$–$ZnCo_2O_4$/CC (b), MoS_2–$ZnCo_2O_4$/CC (c), and MoS_2–$ZnCo_2O_4$–$ZnCo_2O_4$/CC (d) to 1 mM H_2S in PBS (pH 7.4); inset: comparison of peak currents. (C) CVs of MoS_2–$ZnCo_2O_4$–$ZnCo_2O_4$/CC toward 1 mM H_2S under normal (dark teal curve) and bending (red curve) conditions. To keep the bending conditions, the electrode was bent 30 times before taking measurements.

At MoS_2 sites,

$$Mo(\text{IV})S_2 + H_2S \leftrightarrow Mo(\text{II})S_2 + S \quad (16)$$

At $ZnCo_2O_4$ sites,

$$ZnCo_2O_4 + H_2O + e^- \leftrightarrow CoOOH + Zn(OH)^- \quad (17)$$

$$CoOOH + H_2S \leftrightarrow CoO_2 + S + OH^- \quad (18)$$

$$ZnOH + OH^- \leftrightarrow Zn(OH)_2 \quad (19)$$

Next, the ability of the electrode to determine H_2S under bending conditions was tested. Fig. 6C shows the CV curves of MoS_2–$ZnCo_2O_4$–$ZnCo_2O_4$/CC towards 1 mM H_2S under normal and bending conditions. The electrode was bent by twisting to 180 degrees 20 times to make bending deformation. About 95% of the initial H_2S oxidation peak current was retained for the bending electrode compared to the normal electrode, which suggests that the electrode has the ability to produce reproducible signals under strained conditions. These results indicate good flexibility and mechanical stability of the electrode, which can be correlated with the properties of carbon cloth and mechanical adhesion of the material with a carbon cloth electrode. The electrode can be used to fabricate flexible H_2S sensors.

A high stability electrode is needed for continuous monitoring because the electrode has to be in contact with the analyte for hours or even days. To investigate the stability of MoS_2–$ZnCo_2O_4$–$ZnCo_2O_4$/CC, its H_2S sensing capacity was monitored every day by analyzing catalytic responses periodically. The electrode showed approximately 94.3% of its initial current response after the tenth day of its continuous use, suggesting appreciable stability (Fig. S1A, ESI†). The stability result suggests that the material has good mechanical adhesion on the surface of carbon cloth. It is known that direct growth of materials on the carbon cloth electrode can provide good mechanical adhesion and excellent conductivities, which in turn enable high selectivity for the resulting sensor.[46,47] Reproducibility of the MoS_2–$ZnCo_2O_4$–$ZnCo_2O_4$/CC was tested by conducting CV experiments towards 1 mM H_2S. The sensor displayed good reproducibility with an R.S.D. of 3.9% for five individual electrodes (Fig. S1B, ESI†). A possible explanation for the appreciable reproducibility and anti-fouling property of the electrode can be postulated in terms of repulsive forces between the sulfur layers of MoS_2 and the elemental sulfur of the H_2S-oxidized product. MoS_2 sheets contain a layer of Mo atoms sandwiched between two layers of S atoms.[48] When elemental sulfur produced by H_2S oxidation reaches the electrode surface, it confronts with the sulfur layers of MoS_2 at the interface region, where it is most likely to experience a repulsive interaction. This interaction imposes the elemental sulfur to divert to the bulk solution region, thus preventing the fouling of the interface region.

The effects of H_2S concentration, scan rate, and pH are given in the ESI.† The effect of concentration confirms good anti-poisoning nature of the film (Fig. S2A and B, ESI†). The effect of scan rate suggests a diffusion controlled oxidation process (Fig. S3A and B, ESI†). The effect of pH suggests that pH 7.4 is the optimum pH for maximum H_2S sensing performance (Fig. S4A–C, ESI†).

3.6. High sensitivity and selectivity

A chronoamperometric method was used to investigate the H_2S determination capabilities of unmodified CC, $ZnCo_2O_4$–$ZnCo_2O_4$/CC, MoS_2–$ZnCo_2O_4$/CC and MoS_2–$ZnCo_2O_4$–$ZnCo_2O_4$/CC. The electrode potential was +0.20 V (*vs.* Ag/AgCl). As shown in Fig. 7A, the MoS_2–$ZnCo_2O_4$–$ZnCo_2O_4$/CC displayed superior chronoamperometric response to sense H_2S compared to the control electrodes. Next, the response of MoS_2–$ZnCo_2O_4$–$ZnCo_2O_4$/CC toward different concentrations of H_2S was tested (Fig. 7B). Well-defined and quick responses were obtained for each concentration of H_2S and a good linear relationship was observed between current and [H_2S]. Next, chronoamperometric experiments were conducted from the nanomolar to millimolar range to find the sensor's working range, which was found to be 10 nM–1000 μM (Fig. 7C). The limit of detection (LOD) was estimated to be 5 nM. The LOD was calculated using the formula LOD = $3s_b/S$ (where s_b = standard deviation of 10 blank signals and S = sensitivity).

As can be seen from Table 1, the MoS_2–$ZnCo_2O_4$–$ZnCo_2O_4$/CC shows relatively better performance than many of the existing methods. This is mainly because the double-layered $ZnCo_2O_4$ and MoS_2 nanostructured materials provide large surface area, and excellent electrocatalytic and electron shuttling properties. Although the electrode potentials of enzymatic biosensors are slightly better than our method, their use in continuous monitoring systems is still limited because fragile bio-components negatively affect the sensor's life.[53] Some reports use highly acidic or alkaline pH conditions; but these extreme treatments cause false positives or false negatives.[56] Besides, most of the previous reports mainly focused on environmental or serum samples, but were not used in live biological systems such as *E. coli*. In contrast, the MoS_2–$ZnCo_2O_4$–$ZnCo_2O_4$/CC sensor has several advantages, such as working at decent potential, operating at physiological pH, and detecting *in situ* H_2S from live biological media.

Next, the selectivity of the MoS_2–$ZnCo_2O_4$–$ZnCo_2O_4$/CC was tested by monitoring its sensing performance in the presence

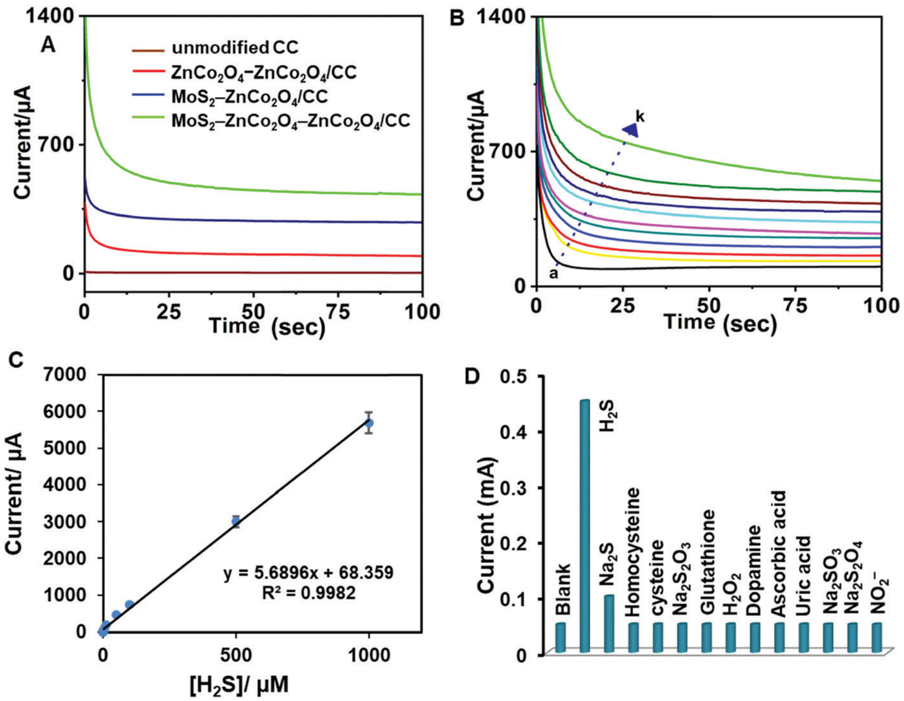

Fig. 7 (A) Chronoamperometric responses of unmodified CC (brown), $ZnCo_2O_4$–$ZnCo_2O_4$/CC (red), MoS_2–$ZnCo_2O_4$/CC (blue), and MoS_2–$ZnCo_2O_4$–$ZnCo_2O_4$/CC (green) electrodes in the presence of 1 μM H_2S, applied potential = +0.20 V (*vs.* Ag/AgCl). (B) Chronoamperometric responses of MoS_2–$ZnCo_2O_4$–$ZnCo_2O_4$/CC to H_2S (a to k; 0 to 100 μM). (C) Linear regression plot: current/mA *vs.* [H_2S]/μM. (D) Bar chart for selectivity of MoS_2–$ZnCo_2O_4$–$ZnCo_2O_4$/CC, evaluated from its amperometric response towards 100 μM H_2S and 250 μM of homocysteine, cysteine, $Na_2S_2O_3$, glutathione, H_2O_2, dopamine, ascorbic acid, uric acid, Na_2SO_3, $Na_2S_2O_4$, NO_2^-, and NO dispersed in PBS, pH 7.4.

of likely interfering agents that are commonly coexisting in biological media (Fig. S5, ESI†). 100 μM H_2S and 250 μM of homocysteine, cysteine, $Na_2S_2O_3$, glutathione, H_2O_2, dopamine, ascorbic acid, uric acid, Na_2SO_3, $Na_2S_2O_4$, NO_2^-, and NO have been used. From the bar chart displayed in Fig. 7D, we infer that the electrode responded exclusively to H_2S, but not to other compounds. Irrespective of their 2.5-fold excessive presence in the medium, the signal contribution of other analytes is less than 5%. The selective nature of the film can be explained based on the properties of the materials, which are elaborated below:

(1) The thin coating of POPD provides selective permeability to H_2S. H_2S can penetrate through the film due to its size matching with the pores of POPD. Thiols and other biological species are unable to permeate the POPD film because of their large sizes.[57] It is worth mentioning that, traditional ion selective electrodes encounter severe interference by wrongly counted biothiols.[56] Interestingly, the described electrode eliminates the signal from such biothiols.

(2) The film retains a net positive charge, which rejects positively charged molecules such as dopamine and uric acid *via* electrostatic repulsive interactions.

(3) H_2S at unmodified electrodes usually requires high positive potentials ($>+0.4$ V) for oxidation, but higher potential allows interference from unwanted biological species. H_2S oxidation at MoS_2–$ZnCo_2O_4$–$ZnCo_2O_4$/CC occurs at a minimized overpotential, +0.20 V *vs.* Ag/AgCl. On the other hand, a previous report demonstrated that POPD has permeability to H_2O_2; in contrast, here we do not see any notable signal for H_2O_2.[57] This is because of the differences in electrode potential requirements between H_2O_2 and H_2S. Although H_2O_2 has the ability to reach the electrode, it requires high positive potentials. Thus, the use of a minimized overpotential has contributed significantly to the electrode's selectivity.

3.7. Practical applicability in whole blood, fetal bovine serum and *E. coli*

The practical sensing performance of MoS_2–$ZnCo_2O_4$–$ZnCo_2O_4$/CC demonstrated in human blood (A), LB medium (B), *E. coli* (C) and fetal bovine serum (D) have been tested (Fig. 8). Whole samples were tested without any pre-treatments. These media have been found to be H_2S-free and then known amounts of H_2S (*i.e.*, NaHS) were spiked and the resulting spiked samples were analyzed by chronoamperometry. Regardless of the presence of other biological compounds in the aforementioned biological fluids, our method can accurately measure the amount of H_2S produced, indicating its best practical applicability in major biological fluids.

3.8. Real-time tracking of H_2S production in *E. coli*

H_2S is endogenously produced by bacterial cells as a common defense agent against antibiotics.[58] H_2S protects the bacteria from oxidative stress and antibiotics by suppressing DNA breakdown and enhancing the activity of catalase and superoxide dismutase.[59] It is well known that H_2S is biosynthesized from cysteine; therefore cysteine can be used as a stimulant to induce the cells to produce H_2S. Fig. 8E displays the chronoamperometric responses of the MoS_2–$ZnCo_2O_4$–$ZnCo_2O_4$/CC to *E. coli* in the presence (green curve) and absence (red curve) of cysteine. A steady background current was observed in the absence of stimulant; however, a sharp increase in the chronoamperometric current was observed with stimulant. Here, the cysteine supplementation stimulated the *E. coli* to produce H_2S endogenously, and the as-produced H_2S transported to the interface *via* diffusion and subsequently electrocatalyzed by the interface. The amount of H_2S release is directly proportional to the response current. Control experiments such as analysis in only LB medium and LB medium + cysteine have shown just baseline.

Next, the MoS_2–$ZnCo_2O_4$–$ZnCo_2O_4$/CC was employed to track dynamic endogenous H_2S production with respect to stimulation time. The experimental curves are given in ESI,† Fig. S6, while the corresponding real-time plot is given in Fig. 8F. 0.5 mM cysteine was supplemented to *E. coli* (2.5×10^9 cells per mL), maintained at 37 °C, and the amperometric signal was tracked for a time span of 30 min to 330 min. During the resting time, the electrochemical cell was tightly capped and maintained at 37 °C. The current signal was plotted against time (red lines, Fig. 8F). As per the plot, the response current was increased significantly from 0–60 min, indicating the linear increase of H_2S liberation. The limiting signal reached maxima at 60 min, indicating that the maximum H_2S production was achieved. The signal however followed a declining trend from 60–180 min, dropped to baseline at 210 min, which indicated that the production of H_2S is halted. No obvious current change was noticed from 180 to 240 min. The amount of H_2S was quantified by matching the H_2S tracking profile with the regression plot derived from H_2S quantification carried out in

Table 1 Comparison of the analytical performance of MoS_2–$ZnCo_2O_4$–$ZnCo_2O_4$/CC with previous reports

Electrode (amperometry technique)	Linear range/μM	Detection limit	Real samples	Ref.
Graphene-based 3D scaffold	0.2–10	50 nM	HeLa cells	49
Curcumin-quinone/carbon black	10–1200 10–100	7.12, 2.40 μM	Tap water	50
Pencil graphite electrode/quercetin	1–20, 20–800	0.3 μM	Waste water	51
9,10-Phenanthrenequinone/graphene oxide	1–100, 300–5000	700 nM	Human blood	52
Coprinus cinereus peroxidase/chitosan/SPE biosensor	1.09–16.3	0.3 μM	Environmental water	53
Cu_2O–CuO@Au	0.01–11000	1 nM	Human cell A375	54
V_2O_5/PtIr wire	0.5–15	0.5 μM	—	55
MoS_2–$ZnCo_2O_4$–$ZnCo_2O_4$/CC	0.01–1000	5 nM	*E. coli*, human whole blood, fetal bovine serum	This work

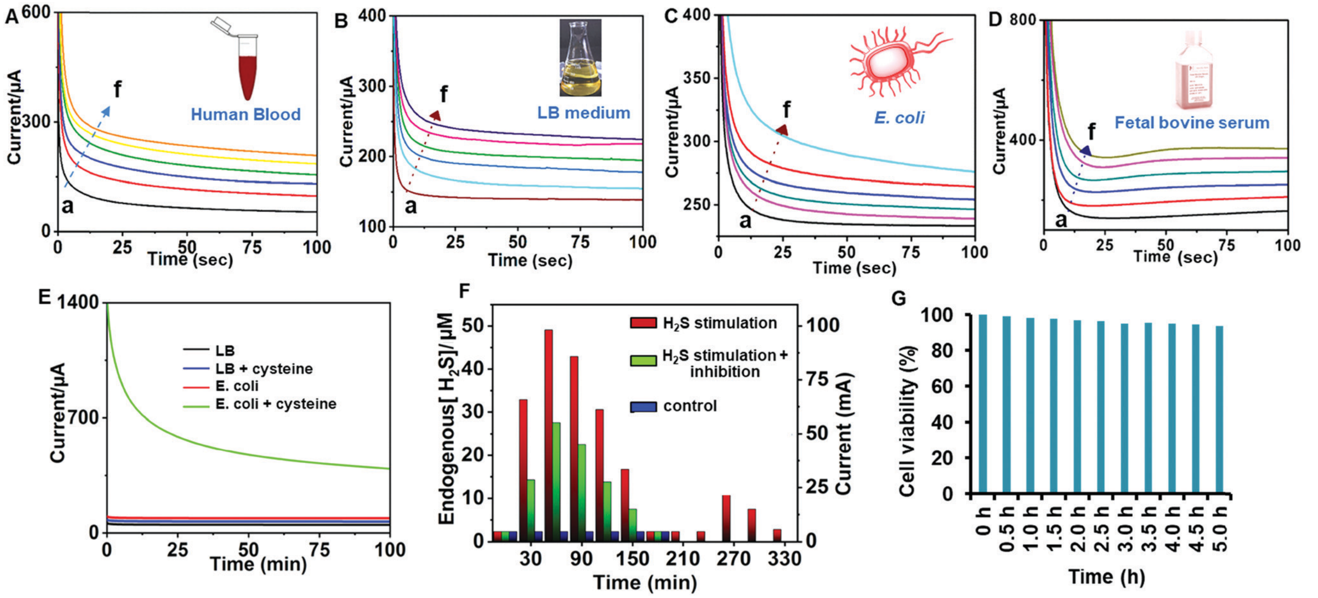

Fig. 8 Chronoamperometric response of MoS_2–$ZnCo_2O_4$–$ZnCo_2O_4$/CC to various concentrations of H_2S (a = 0, b = 10, c = 20, d = 30, and f = 40 μM) spiked human whole blood (A), LB medium (B), *E. coli* (C), and fetal bovine serum (D) suspended in 0.1 M PBS (pH 7.4). Electrode potential = +0.20 V (*vs.* Ag/AgCl). (E) Chronoamperometric response of MoS_2–$ZnCo_2O_4$–$ZnCo_2O_4$/CC to *E. coli* suspended in an LB medium (pH 7.4) at 37 °C without stimulation (red curve), and stimulated with 0.5 mM cysteine (green curve), LB + 0.5 mM cysteine (blue curve), and LB (black curve). (F) Real-time tracking plot: Normalized current responses *vs.* [endogenous H_2S] *vs.* time. H_2S release from *E. coli* suspended in LB Medium at pH 7.4, stimulated by 1 mM cysteine (red lines), stimulated by 1 mM cysteine + 10 mM aspartate (green lines) and with no stimulation (blue lines). (G) Cell viability test.

E. coli via a spiking method. After 240 min, H_2S production was stimulated again by spiking 0.5 mM cysteine in the reaction mixture and real-time monitoring is resumed. The current was steadily increased again for the next 30 min (240 to 270 min) and dropped after 60 min. However, the control experiments without bacteria or without cysteine have only shown baseline under the same conditions. Next, the production of H_2S production was inhibited by a mixture of cysteine and aspartate (H_2S inhibitor) to *E. coli*. The H_2S release trend is similar to the stimulation plot but with suppressed signals (green lines, Fig. 8F). About 40% reduction in current signal was observed in the presence of aspartate, which makes sense since a high concentration of aspartate inhibits the production of H_2S. In the absence of stimulation, the cells showed no response (blue lines, Fig. 8F). Therefore, a pattern of H_2S production is established and any deviation in this triggers an alarm suggesting to check or repair H_2S production systems. Our method works on opaque samples without requiring pre-treatments, involving a simpler assay procedure, and depends on an easier electrode preparation strategy. A cell viability test was performed to investigate the biocompatibility of the electrode. The MoS_2–$ZnCo_2O_4$–$ZnCo_2O_4$/CC electrode was transferred to an electrochemical cell containing *E. coli* cells and incubated for a total of 5 h. Response currents were recorded for each 30 minutes (Fig. 8G). The cell viability of 94% was observed after 5 h of continuous incubation, indicating that the cells were healthy. The use of POPD coating in electrode fabrication is the main reason for the electrode's good biocompatibility. Several previous studies proved that POPD has good anti-biofouling properties in proteinaceous media due to its greater compactness.[60]

4. Conclusions

In summary, a robust, sensitive carbon cloth electrode modified with MoS_2–$ZnCo_2O_4$–$ZnCo_2O_4$ is developed for real-time *in situ* sensing of H_2S in biological media. The double-layered $ZnCo_2O_4$ has better surface properties than single-layered $ZnCo_2O_4$ and it can produce dense and uniform MoS_2 structures with advanced porous and roughened catalytic sites. MoS_2–$ZnCo_2O_4$–$ZnCo_2O_4$/CC has relatively better electrochemical properties, high electrochemical active area and lower interfacial electron transfer resistance compared to MoS_2–$ZnCo_2O_4$/CC. In addition, the electrode has excellent H_2S sensing ability, anti-poisoning properties, wide linear range (0.01–1000 μM), low detection limit (5 nM), and good selectivity (2.5 fold). The method is practically applicable in human blood, fetal bovine serum, and *E. coli* cells. MoS_2–$ZnCo_2O_4$–$ZnCo_2O_4$/CC can be used for accurate quantification of endogenous H_2S production in bacterial cells, continuously for up to 5 hours. The method would be an effective diagnostic tool for biomedical applications in a point-of-care setting and the use of flexible substrate leaves the possibility of extending its applicability to stretchable biosensors.

Conflicts of interest

The authors declare that they have no competing interests.

Acknowledgements

This work was supported by the Ministry of Science and Technology (107-2113-M-027-007- and 108-2221-E-027-063-), Taiwan and King Abdullah University of Science and Technology (KAUST), Saudi Arabia. We also thank the support from Japanese Government MONBUKAGAKUSHO: MEXT Scholarship.

References

1 G. Rong, S. R. Corrie and H. A. Clark, *ACS Sens.*, 2017, **2**, 327–338.

2 G. S. Wilson and R. Gifford, *Biosens. Bioelectron.*, 2005, **20**, 2388–2403.

3 M. Asif, W. Haitao, D. Shuang, A. Aziz, G. Zhang, F. Xiao and H. Liu, *Sens. Actuators, B*, 2017, **239**, 243–252.

4 H. Yang, Y. Zhang, L. Li, G. Sun, L. Zhang, S. Ge and J. Yu, *Biosens. Bioelectron.*, 2017, **87**, 53–58.

5 A. R. Lippert, E. J. New and C. J. Chang, *J. Am. Chem. Soc.*, 2011, **133**, 10078–10080.

6 H. Kimura, *Neurochem. Int.*, 2013, **63**, 492–497.

7 T. Xu, N. Scafa, L.-P. Xu, S. Zhou, K. Abdullah Al-Ghanem, S. Mahboob, B. Fugetsu and X. Zhang, *Analyst*, 2016, **141**, 1185–1195.

8 P. D. Tran, T. V. Tran, M. Orio, S. Torelli, Q. D. Truong, K. Nayuki, Y. Sasaki, S. Y. Chiam, R. Yi and I. Honma, *Nat. Mater.*, 2016, **15**, 640–646.

9 O. Yassine, O. Shekhah, A. H. Assen, Y. Belmabkhout, K. N. Salama and M. Eddaoudi, *Angew. Chem., Int. Ed.*, 2016, **55**, 15879–15883.

10 E. A. Peter, X. Shen, S. H. Shah, S. Pardue, J. D. Glawe, W. W. Zhang, P. Reddy, N. I. Akkus, J. Varma and C. G. Kevil, *J. Am. Heart Assoc.*, 2013, **2**, e000387.

11 M. Dulac, A. Melet and E. Galardon, *ACS Sens.*, 2018, **3**, 2138–2144.

12 A. M. O'Mahony, E. J. Dickinson, L. Aldous, C. Hardacre and R. G. Compton, *J. Phys. Chem. C*, 2009, **113**, 10997–11002.

13 M. Asif, H. Liu, A. Aziz, H. Wang, Z. Wang, M. Ajmal, F. Xiao and H. Liu, *Biosens. Bioelectron.*, 2017, **97**, 352–359.

14 M. Asif, A. Aziz, M. Azeem, Z. Wang, G. Ashraf, F. Xiao, X. Chen and H. Liu, *Adv. Colloid Interface Sci.*, 2018, **262**, 21–38.

15 M. D. Brown, J. R. Hall and M. H. Schoenfisch, *Anal. Chim. Acta*, 2019, **1045**, 67–76.

16 N. Wongkaew, M. Simsek, C. Griesche and A. J. Baeumner, *Chem. Rev.*, 2018, **119**, 120–194.

17 M. Asif, A. Aziz, Z. Wang, G. Ashraf, J. Wang, H. Luo, X. Chen, F. Xiao and H. Liu, *Anal. Chem.*, 2019, **91**, 3912–3920.

18 X. B. Hu, Y. L. Liu, H. W. Zhang, C. Xiao, Y. Qin, H. H. Duo, J. Q. Xu, S. Guo, D. W. Pang and W. H. Huang, *ChemElectroChem*, 2016, **3**, 1998–2002.

19 Y. Sharma, N. Sharma, G. Subba Rao and B. Chowdari, *Adv. Funct. Mater.*, 2007, **17**, 2855–2861.

20 S. Sahoo and J.-J. Shim, *ACS Sustainable Chem. Eng.*, 2017, **5**, 241–251.

21 S. G. Surya, S. M. Majhi, D. K. Agarwal, A. A. Lahcen, S. Yuvaraja, K. N. Chappanda and K. N. Salama, *J. Mater. Chem. B*, 2020, **8**, 18–26.

22 W. Luo, X. Hu, Y. Sun and Y. Huang, *J. Mater. Chem.*, 2012, **22**, 8916–8921.

23 Y. Gai, Y. Shang, L. Gong, L. Su, L. Hao, F. Dong and J. Li, *RSC Adv.*, 2017, **7**, 1038–1044.

24 W. Bai, H. Tong, Z. Gao, S. Yue, S. Xing, S. Dong, L. Shen, J. He, X. Zhang and Y. Liang, *J. Mater. Chem. A*, 2015, **3**, 21891–21898.

25 X. Ge, Z. Li, C. Wang and L. Yin, *ACS Appl. Mater. Interfaces*, 2015, **7**, 26633–26642.

26 I. K. Moon, S. Yoon and J. Oh, *Chem. – Eur. J.*, 2017, **23**, 597–604.

27 H. Long, A. Harley-Trochimczyk, S. Cheng, H. Hu, W. S. Chi, A. Rao, C. Carraro, T. Shi, Z. Tang and R. Maboudian, *ACS Appl. Mater. Interfaces*, 2016, **8**, 31764–31771.

28 J. Zhang, S. Cui, Y. Ding, X. Yang, K. Guo and J.-T. Zhao, *Biosens. Bioelectron.*, 2018, **112**, 177–185.

29 V. Mani, S. Selvaraj, T.-K. Peng, H.-Y. Lin, N. Jeromiyas, H. Ikeda, Y. Hayakawa, S. Ponnusamy, C. Muthamizhchelvan and S.-T. Huang, *ACS Appl. Nano Mater.*, 2019, **2**, 5049–5060.

30 J. R. Hall and M. H. Schoenfisch, *Anal. Chem.*, 2018, **90**, 5194–5200.

31 M. Pumera and A. H. Loo, *TrAC, Trends Anal. Chem.*, 2014, **61**, 49–53.

32 Y. Zhang, Z. Hu, Y. Liang, Y. Yang, N. An, Z. Li and H. Wu, *J. Mater. Chem. A*, 2015, **3**, 15057–15067.

33 S. Madhu, A. J. Anthuuvan, S. Ramasamy, P. Manickam, S. Bhansali, P. Nagamony and V. Chinnuswamy, *ACS Appl. Electron. Mater.*, 2020, **2**, 499–509.

34 L. Shen, Q. Che, H. Li and X. Zhang, *Adv. Funct. Mater.*, 2014, **24**, 2630–2637.

35 M. Zhen, X. Zhang and L. Liu, *RSC Adv.*, 2016, **6**, 43551–43555.

36 Y. Zhou, G. Liu, X. Zhu and Y. Guo, *Sens. Actuators, B*, 2017, **251**, 280–290.

37 S. Sahoo and J.-J. Shim, *ACS Sustainable Chem. Eng.*, 2016, **5**, 241–251.

38 D. Dinda, M. E. Ahmed, S. Mandal, B. Mondal and S. K. Saha, *J. Mater. Chem. A*, 2016, **4**, 15486–15493.

39 J. Cheng, H. Yan, Y. Lu, K. Qiu, X. Hou, J. Xu, L. Han, X. Liu, J.-K. Kim and Y. Luo, *J. Mater. Chem. A*, 2015, **3**, 9769–9776.

40 X.-C. Dong, H. Xu, X.-W. Wang, Y.-X. Huang, M. B. Chan-Park, H. Zhang, L.-H. Wang, W. Huang and P. Chen, *ACS Nano*, 2012, **6**, 3206–3213.

41 W. Zhou, D. Kong, X. Jia, C. Ding, C. Cheng and G. Wen, *J. Mater. Chem. A*, 2014, **2**, 6310–6315.

42 A. Aziz, M. Asif, M. Azeem, G. Ashraf, Z. Wang, F. Xiao and H. Liu, *Anal. Chim. Acta*, 2019, **1047**, 197–207.

43 M. Asif, A. Aziz, H. Wang, Z. Wang, W. Wang, M. Ajmal, F. Xiao, X. Chen and H. Liu, *Microchim. Acta*, 2019, **186**, 61.

44 P. Tamilarasan and S. Ramaprabhu, *J. Mater. Chem. A*, 2014, **2**, 14054–14063.

45 B. Dinesh, K. S. Shalini Devi and A. S. Kumar, *J. Electroanal. Chem.*, 2017, **804**, 116–127.

46 E. Scavetta, A. Casagrande, I. Gualandi and D. Tonelli, *J. Electroanal. Chem.*, 2014, **722-723**, 15–22.

47 J. Cheng, Y. Lu, K. Qiu, H. Yan, X. Hou, J. Xu, L. Han, X. Liu, J.-K. Kim and Y. Luo, *Phys. Chem. Chem. Phys.*, 2015, **17**, 17016–17022.

48 Y. Fang, J. Pan, J. He, R. Luo, D. Wang, X. Che, K. Bu, W. Zhao, P. Liu and G. Mu, *Angew. Chem., Int. Ed.*, 2018, **130**, 1246–1249.

49 X.-B. Hu, Y.-L. Liu, W.-J. Wang, H.-W. Zhang, Y. Qin, S. Guo, X.-W. Zhang, L. Fu and W.-H. Huang, *Anal. Chem.*, 2018, **90**, 1136–1141.

50 B. Dinesh, K. S. Devi and A. S. Kumar, *J. Electroanal. Chem.*, 2017, **804**, 116–127.

51 Y. Dilgin, B. Kızılkaya, B. Ertek, N. Eren and D. G. Dilgin, *Talanta*, 2012, **89**, 490–495.

52 K. S. Devi and A. S. Kumar, *Analyst*, 2018, **143**, 3114–3123.

53 I. S. P. Savizi, H.-R. Kariminia, M. Ghadiri and R. Roosta-Azad, *Biosens. Bioelectron.*, 2012, **35**, 297–301.

54 M. Asif, A. Aziz, G. Ashraf, Z. Wang, J. Wang, M. Azeem, X. Chen, F. Xiao and H. Liu, *ACS Appl. Mater. Interfaces*, 2018, **10**, 36675–36685.

55 J. A. Bennett, J. E. Pander III and M. A. Neiswonger, *J. Electroanal. Chem.*, 2011, **654**, 1–7.

56 K. R. Olson, E. R. DeLeon and F. Liu, *Nitric oxide*, 2014, **41**, 11–26.

57 Y.-Q. Dai, D.-M. Zhou and K.-K. Shiu, *Electrochim. Acta*, 2006, **52**, 297–303.

58 K. Shatalin, E. Shatalina, A. Mironov and E. Nudler, *Science*, 2011, **334**, 986–990.

59 H. Kimura, *Antioxid. Redox Signaling*, 2014, **20**, 783–793.

60 M. D. Brown and M. H. Schoenfisch, *ACS Sens.*, 2016, **1**, 1453–1461.